

## Research Article

<https://doi.org/10.1631/jzus.A2300373>



# A novel shear damage model of the shear deformation and failure process of gas hydrate-bearing sediments

Hui WANG<sup>1,2</sup>, Bo ZHOU<sup>1</sup>✉

<sup>1</sup>College of Pipeline and Civil Engineering, China University of Petroleum (East China), Qingdao 266580, China

<sup>2</sup>Institute of Water Engineering Sciences, Wuhan University, Wuhan 430072, China

**Abstract:** A novel shear damage model based on homogenization theory and a modified Mohr-Coulomb criterion is proposed to predict the full deformation process of gas hydrate-bearing sediments (GHBSs) during shearing by analyzing micro-mechanisms of shear deformation and failure characteristics. Then, the physical significance of the model's parameters is explored. Finally, the damage evolution and shear stress partition inside GHBSs during the shearing process are analyzed in detail. The results show that model parameters have clear physical meaning, and the shear damage model is capable of reflecting the nonlinear deformation and strain softening characteristics of GHBSs due to its ability to better describe the damage evolution and shear stress partition mechanisms inside GHBSs during the shearing process. Comparisons of experimental and theoretical results show that the global performance of the novel shear damage model is satisfactory. The model is expected to be widely adopted to analyze submarine landslide instability due to hydrate dissociation.

**Key words:** Gas hydrate-bearing sediments (GHBSs); Shear damage model; Homogenization theory; Modified Mohr-Coulomb (MC) criterion; Damage evolution

## 1 Introduction

Gas hydrate (GH) is commonly found in permafrost layers and deep sea beds (Stern et al., 1998; Kvenvolden, 1999; Sloan Jr, 2003; Brugada et al., 2010). As the most promising clean energy source for the future, the safe extraction of GH has drawn increasing interest from all over the world (Kvenvolden, 1998; Yang et al., 2014). However, excessive dissociation of GH in the pore spaces of the sediment matrix due to the use of immature exploitation technology may lead to submarine landslide and wellbore collapse (Sloan Jr and Koh, 2007; Jia et al., 2016; Zhu et al., 2017). Furthermore, the escape of methane gas that is 20–30 times more potent as a greenhouse gas than CO<sub>2</sub> from hydrate reservoirs may contribute to global warming, which could lead to an increase in seawater temperatures. Further temperature increases will further promote ice

melting and methane hydrate dissociation, with a significant influence on the global carbon cycle and climate change (Farahani et al., 2021a, 2021b).

In the past decade, most research has focused on the effects of the degree of saturation of GH (Masui et al., 2005; Miyazaki et al., 2011; Yoneda et al., 2015), effective confining pressure (Yu et al., 2011), strain rate (Deusner et al., 2019), GH morphology (Hyodo et al., 2013a), temperature (Song et al., 2016; Liu et al., 2017), pore pressure (Hyodo et al., 2013b), fine-grained content (Hyodo et al., 2017; Li DL et al., 2019), sediment types (Yun et al., 2007; Kajiyama et al., 2017), and hydrate dissociation (Hyodo et al., 2014; Luo et al., 2020) on the peak strength and deformation characteristics of gas hydrate-bearing sediments (GHBSs). These studies have involved carrying out a series of triaxial compression tests, direct shear tests, and plane strain tests. With the continuous development of laboratory visualization technology, the microstructural evolution under loading and environmental conditions has been more comprehensively studied using X-ray computed tomography (CT) (Yoneda et al., 2016; Wu et al., 2020), magnetic resonance imaging (MRI) (Song et al., 2015;

✉ Bo ZHOU, zhoubo@upc.edu.cn

 Bo ZHOU, <https://orcid.org/0000-0003-2989-1137>

Received July 21, 2023; Revision accepted Dec. 2, 2023;  
Crosschecked Dec. 22, 2024; Online first Jan. 18, 2025

© Zhejiang University Press 2025

Ji et al., 2019), and Cryo scanning electron microscopy (Hou et al., 2018). Meanwhile, the discrete element method (DEM) was introduced to explore mesoscopic deformation and particle-scale motion from a microscopic perspective (Jiang et al., 2014, 2019; Xu et al., 2016).

Based on a large number of experimental and DEM simulation findings, several constitutive models were proposed to describe the nonlinear and strain softening characteristics of GHBSs. Many attempts have been made to capture the unique mechanical characteristics of GHBSs, which are regarded as homogeneous and isotropic geotechnical materials. The models used include the Duncan-Chang model (Miyazaki et al., 2012; Yan et al., 2017), Mohr-Coulomb (MC) plastic model (Pinkert et al., 2015; Pinkert, 2017), critical state model (Uchida et al., 2016; Zhou et al., 2018), state-dependent constitutive model (Shen et al., 2016; Ng et al., 2020, 2023; Fang et al., 2022), granular thermodynamic model (Bai et al., 2023), and hypoplastic model (Zhang et al., 2018). Note that these constitutive models were proposed from a phenomenological perspective, which cannot explain the microscopic mechanisms of the failure and deformation of GHBSs. In contrast, some researchers considered GHBSs as a composite geomaterial consisting of sediment matrix, GH particles, pore fluid, and methane gas. Hence, by hypothesizing that the external loading of hydrate-bearing sediments is jointly carried by two components, namely the sediment matrix and methane hydrate, a stress partition constitutive framework for methane hydrate-bearing sediment (SPF-MHBS) was established based on the concept of stress partition (Wang et al., 2023; Xu et al., 2023). Zhang N et al. (2022) proposed a mesoelastic-plastic damage mechanical model for MHBSs by introducing statistical damage theory and Gurson plastic damage theory and considering various hydrate growth patterns. Although the above meso-mechanical constitutive models of GHBSs can better model the mesoscopic structural evolution under loading, there is an accompanying increase in the number of model parameters, some of which lack physical meanings. Submarine landslides are a progressive failure process, which is accompanied by strain hardening after yielding and post-peak softening characteristics (Skempton, 1985). Hence, to rapidly evaluate the instability of submarine slopes due to GH dissociation, it is more important to establish a shear model that

can describe the shear stress–shear displacement curves, including the full shear deformation and failure process. There was no relevant theory of the shear model for GHBSs, and so this was an essential motivation for this study.

In this paper, the characteristics and micro-mechanism of shear deformation of GHBSs in direct shear tests are summarized first. A shear damage model based on homogenization theory and a modified MC criterion is proposed to predict the shear stress–shear displacement curves of GHBSs in the direct shear tests. Then, the physical significance of the shear damage model parameters is investigated. Finally, the novel shear damage model is used to describe the evolution of damage and shear stress partition mechanisms inside GHBSs.

## 2 Characteristics and micro-mechanism of shear deformation

GHBSs (Fig. 1) are composed of GH particles, sand particles, methane gas, and water. Therefore, the mechanical characteristics of the microscopic components and the interaction between them predominantly determine the macroscopic mechanical behavior of the sediments. Fig. 2 depicts a typical diagram of shear stress–shear displacement curve of GHBSs, which may be divided into five stages:

(1) Elastic deformation stage (stage *OA*): in the early stages of *OA*, shear stress increases linearly with increasing displacements. As a result, the deformation

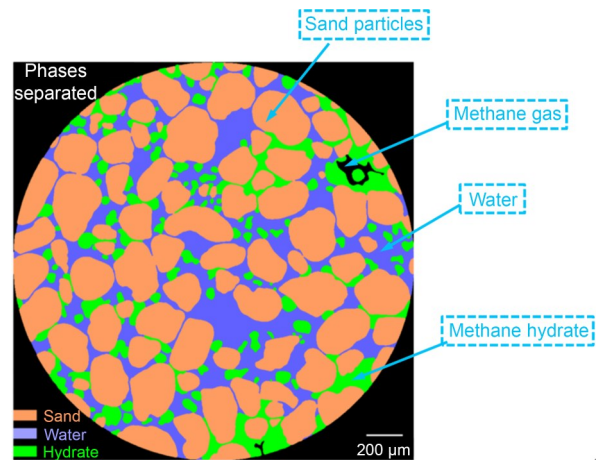
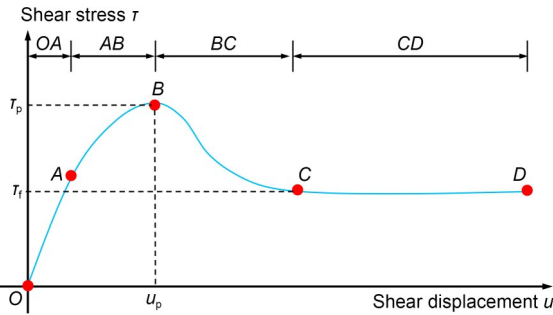


Fig. 1 CT results of GHBSs (Lei et al., 2019). References to color refer to the online version of this figure



**Fig. 2 Representative shear constitutive relationship of GHBSs (Liu et al., 2017, 2018)**

at this stage is categorized as elastic deformation. The macroscopic phenomena are explained by the absence of hydrate bond breakage at the particle scale.

(2) Yield hardening stage (stage AB): after passing over point A, the shear stress curve becomes convex rather than straight. Point A, the initial yield point, represents the transition from the elastic stage to the plastic hardening stage. This occurs because hydrate bonds break at random in GHBSs under external stress, resulting in the slipping and rotation of sand particles.

(3) Strain softening stage (stage BC): after the peak strength point (peak shear stress  $\tau_p$  at shear displacement  $u_p$  corresponding to point B), with an increase in displacement, shear stress decreases rapidly from peak shear stress to residual shear stress ( $\tau_r$ ). The loss of cohesion strength inside sediments, which results from the breakage of hydrate bonds, is the primary cause of a decrease in shear stress (strain softening).

(4) Residual strength stage (stage CD): when shear stress reaches this point, which is independent of displacement, it remains constant. The constant shear stress during the stage is defined as the residual shear stress. From a microscopic perspective, friction at the interface between hydrate particles and sand particles contributes to the residual shear stress of GHBSs.

Table 1 depicts particle-scale mechanisms of GHBSs with different saturations under shearing. As GH saturation ( $S_{GH}$ ) increases, hydrates have various effects on the sliding and rotation of sand particles, resulting in an increase in the macroscopic residual shear stress of GHBSs. Also, the hydrate pore morphology plays a different role in hydrate deformation and failure. When the GH saturation is less than 25%, the hydrate mostly fills the pores in a pore-filling type, which increases the shear stress of GHBSs by increasing the frictional resistance of sand particle surfaces. When the GH saturation is greater than 40%, the hydrate in the

**Table 1 Particle-scale mechanisms of GHBSs under shearing (Liu et al., 2017; Yun et al., 2007)**

$S_{GH}$	Item	Initial state	Mechanism in movement	
			Slip	Rotation
0%				
<25%	Pore filling			
>40%	Grain coating			
>40%	Cementing			

pore spaces is mostly in the form of cementation and grain coating, which mainly increases the shear stress and resistance to deformation by cementing the neighboring sand particles and increasing the friction on the surface of sand particles. In a permafrost region, the presence of ice can cement two adjacent sand particles together to form stronger cemented clusters, thereby giving the hydrate reservoir a higher strength. At the same time, although GHs are more stable at higher pressures, ice will be melted at higher pressures, which also leads to more settlement deformation of hydrate reservoirs in permafrost regions.

### 3 Shear damage model for GHBSs

#### 3.1 Basic concepts

GHBSs are composite geotechnical materials composed of sediment matrix particles (sand or clay particles), hydrate particles, water, and free methane gas, resulting in complex physical and mechanical characteristics (Lei et al., 2019; Wu et al., 2023). Previous findings have demonstrated that GH particles are mainly bonded and bridged between the sand particles (Chaouachi et al., 2015; Li CF et al., 2019). The presence of natural GH particles results in stronger structural characteristics of sediments. When GHBSs are subjected to external loadings, bond breakage between the GH particles and sand particles gradually occurs. Therefore, GHBSs are divided into two parts: intact parts, called bonded elements, and damaged parts, called frictional

elements (Fig. 3) (Zou et al., 2020). The essence of the evolution of the macroscopic mechanical response of GHBSs is the result of a decrease in the number of bonded elements and an increase in the number of frictional elements inside the sediments. In this study, bonded elements were considered as elastic brittle materials, whereas frictional elements were seen as ideal elastic-plastic materials (Fig. 4) (Xie et al., 2020a, 2020b).

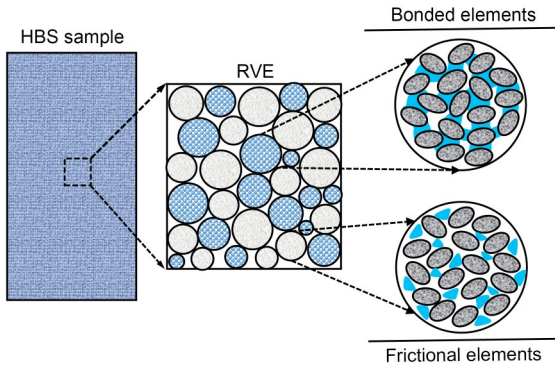


**Fig. 3 Structure model of GHBSs.** HBS represents the hydrate-bearing sediment; RVE represents the representative volume element

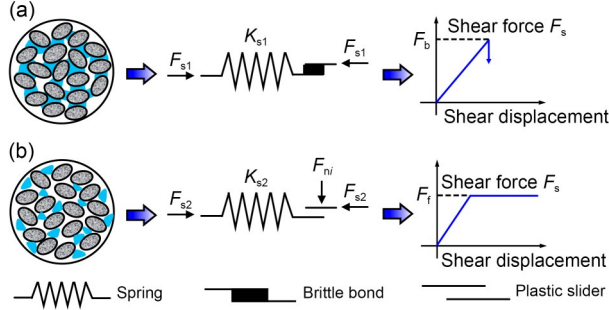


**Fig. 4 Mechanical response of RVE:** (a) bonded elements; (b) frictional elements.  $F_{s1}$  is the shear force of bonded elements;  $F_{s2}$  is the shear force of frictional elements;  $K_{s1}$  is the stiffness of bonded elements;  $K_{s2}$  is the stiffness of frictional elements;  $F_{n1}$  is the normal force of frictional elements;  $F_b$  is the maximum shear force of bonded elements;  $F_f$  is the maximum shear force of frictional elements

Total shear force  $T$  on the shear surface may be expressed using binary medium theory (Zou et al., 2020):

$$T = \left[ \sum_{i=1}^{N_b} (k_b + k_f) u + \sum_{i=1}^{N_f} P_{ni} \tan \phi_i \right] \cdot A, \quad (1)$$

where  $A$  is the area of the shear surface;  $k_b$  and  $k_f$  are the shear stiffnesses of the bonded elements and frictional elements, respectively;  $\phi_i$  is the friction angle of

the frictional elements;  $P_{ni}$  is the normal stress of frictional elements.  $N_b$  and  $N_f$  denote the number of bonded elements and frictional elements, respectively. Then, the average shear stress  $\tau$  on the shear surface can be obtained by dividing both sides by  $A$ , as shown in Eq. (2):

$$\tau = \left[ \sum_{i=1}^{N_b} (k_b + k_f) u + \sum_{i=1}^{N_f} P_{ni} \tan \phi_i \right]. \quad (2)$$

$D$ , a damage variable to characterize the degree of structural deterioration, is defined as the ratio of the number of frictional elements to the total number of micro-elements:

$$D = \frac{N_f}{N_{total}}, \quad (3)$$

where  $N_{total}$  is the total number of micro-elements. When Eq. (3) is substituted into Eq. (2), we obtain:

$$\tau = \tau_b (1 - D) + D \tau_f, \quad (4)$$

where  $\tau_b$  and  $\tau_f$  are the shear stresses of bonded elements and frictional elements, respectively. Substituting  $\tau_b = k_{HBS} u$  into Eq. (4) yields the shear constitutive relationship:

$$\tau = k_{HBS} u (1 - D) + D \tau_f, \quad (5)$$

where  $k_{HBS}$  is the initial shear stiffness of GHBSs.

### 3.2 Damage evolution equation

Research has shown that the strain softening characteristics of GHBSs are directly related to bond breakage between GH particles and sand particles (Wu et al., 2020; Wang et al., 2021). Therefore, the determination of the damage evolution law inside sediments was critical for predicting the accuracy of the constitutive model proposed in the present study. The application of probabilistic methods to describe the damage evolution of geomaterials is now widely accepted. Lai et al. (2008) discovered that the Weibull distribution could more accurately describe the strength distribution of frozen soil than other probabilistic methods. As a result, the Weibull function was used to quantify the progression of damage inside GHBSs. The Weibull distribution's probability density function  $P(F_a)$  is expressed as follows (Hallinan, 1993):

$$P(F_a) = \frac{m}{F_0} \left(\frac{F_a}{F_0}\right)^{m-1} \exp\left[-\left(\frac{F_a}{F_0}\right)^m\right], \quad (6)$$

where  $F_a$  denotes the micro-element strength distribution variable, and  $F_0$  and  $m$  represent the model parameters of the Weibull function. When the stress level  $F$  is reached, the number of damaged micro-elements  $N_f$  may be stated as:

$$N_f = \int N_{\text{total}} P(F_a) dF = N_{\text{total}} \left\{ 1 - \exp\left[-\left(\frac{F_a}{F_0}\right)^m\right] \right\}. \quad (7)$$

The expression of the statistical damage variable  $D$  can be obtained by solving the simultaneous Eqs. (6) and (7):

$$D = \frac{N_f}{N_{\text{total}}} = 1 - \exp\left[-\left(\frac{F_a}{F_0}\right)^m\right]. \quad (8)$$

Eq. (8) is the damage evolution equation of GHBSs.

### 3.3 Determining the strength criterion of micro-elements

The failure criterion of GHBSs can be expressed by the general formula:

$$F_a = f(\tau) - K_0 = 0, \quad (9)$$

where  $f(\tau)$  is the shear strength of HBS, and  $K_0$  is a constant related to material properties. As the external loading increases, the stress state inside the GHBSs changes continuously. If  $f(\tau) > K_0$ , it implies that the micro-elements of GHBSs have been damaged. The strength criterion, which is used to determine the micro-element strength  $F$  of GHBSs, is the key to determining the damage variable  $D$ . Due to its simple parameters, and extensive application in engineering, the MC criterion has been adopted to predict the strength of GHBSs with different hydrate saturation levels (Dong et al., 2020). Its expression is as follows:

$$F_a = \tau - \tau_y = \tau - (\sigma_n \tan \varphi_{\text{HBS}}^y + c_{\text{HBS}}^y), \quad (10)$$

where  $\tau_y$  is the initial yield shear stress,  $\sigma_n$  denotes the normal stress, and  $\varphi_{\text{HBS}}^y$  and  $c_{\text{HBS}}^y$  represent the frictional angle and cohesion in the yield state for GHBSs,

respectively. Substituting Eq. (10) into Eq. (8), the specific form of the damage evolution equation can be obtained as:

$$D = \frac{N_f}{N_{\text{total}}} = \begin{cases} 0, & u < u_y, \\ 1 - \exp\left[-\left(\frac{k_{\text{HBS}}u - \sigma_n \tan \varphi_{\text{HBS}}^y - c_{\text{HBS}}^y}{F_0}\right)^m\right], & u \geq u_y, \end{cases} \quad (11)$$

where  $u_y$  denotes the shear displacement corresponding to the initial yield point. By substituting Eq. (11) into Eq. (5), the shear constitutive model of GHBSs can be expressed as follows:

$$\tau = \begin{cases} k_{\text{HBS}}u \exp\left[-\left(\frac{k_{\text{HBS}}u - \sigma_n \tan \varphi_{\text{HBS}}^y - c_{\text{HBS}}^y}{F_0}\right)^m\right] + \\ \tau_f \left\{ 1 - \exp\left[-\left(\frac{k_{\text{HBS}}u - \sigma_n \tan \varphi_{\text{HBS}}^y - c_{\text{HBS}}^y}{F_0}\right)^m\right] \right\}, & u > u_y, \\ k_{\text{HBS}}u, & u \leq u_y. \end{cases} \quad (12)$$

### 3.4 Derivation of model parameters

#### 3.4.1 Determination of distribution parameters

Weibull model parameters  $F_0$  and  $m$  cannot be obtained from experimental data. Hence, their determination plays a key role in developing a reasonable shear damage model for characterizing the full shear failure process of GHBSs. In this study, the extremum approach was used to calculate the Weibull parameters  $F_0$  and  $m$  (Zou et al., 2020).

Eq. (12) should satisfy the following conditions:

$$\tau \Big|_{u=u_p} = \tau_p, \quad \frac{d\tau}{du} \Big|_{u=u_p, \tau=\tau_p} = 0, \quad (13)$$

where  $\tau_p$  and  $u_p$  denote the peak shear stress and the corresponding displacement, respectively. Substituting Eq. (12) into Eq. (13), we obtain Eqs. (14) and (15):

$$\tau = k_{\text{HBS}}u \left(1 - D \Big|_{u=u_p}\right) + \tau_f D \Big|_{u=u_p} = \tau_p, \quad (14)$$

$$\frac{d\tau}{du} \Big|_{u=u_p} = k_{HBS} \left( 1 - D \Big|_{u=u_p} \right) + \left( \tau_f - k_{HBS} u \Big|_{u=u_p} \right) \frac{\partial D}{\partial u} \Big|_{u=u_p} = 0, \quad (15)$$

where

$$D \Big|_{u=u_p} = 1 - \exp \left[ - \left( \frac{k_{HBS} u_p - \sigma_n \tan \varphi_{HBS}^y - c_{HBS}^y}{F_0} \right)^m \right], \quad (16)$$

$$\frac{\partial D}{\partial u} \Big|_{u=u_p} = \frac{m k_{HBS} (k_{HBS} u_p - \sigma_n \tan \varphi_{HBS}^y - c_{HBS}^y)^{m-1}}{F_0^m} \times \exp \left[ - \left( \frac{k_{HBS} u_p - \sigma_n \tan \varphi_{HBS}^y - c_{HBS}^y}{F_0} \right)^m \right]. \quad (17)$$

Eq. (14) can be simplified as follows:

$$\frac{\tau_p - \tau_f}{\exp \left[ - \left( \frac{k_{HBS} u_p - \sigma_n \tan \varphi_{HBS}^y - c_{HBS}^y}{F_0} \right)^m \right]} = k_{HBS} u_p - \tau_f. \quad (18)$$

Meanwhile, Eq. (15) can also be expressed as:

$$\frac{1}{\frac{m}{F_0} \left( \frac{k_{HBS} u_p - \sigma_n \tan \varphi_{HBS}^y - c_{HBS}^y}{F_0} \right)^{m-1}} = k_{HBS} u_p - \tau_f. \quad (19)$$

Note that the same term  $k_{HBS} u_p - \tau_f$  can be observed in Eqs. (18) and (19). Hence, Eq. (20) can be derived by combining Eqs. (18) and (19):

$$\left( \tau_p - \tau_f \right) \frac{m}{F_0} \left( \frac{k_{HBS} u_p - \sigma_n \tan \varphi_{HBS}^y - c_{HBS}^y}{F_0} \right)^{m-1} = \exp \left[ - \left( \frac{k_{HBS} u_p - \sigma_n \tan \varphi_{HBS}^y - c_{HBS}^y}{F_0} \right)^m \right]. \quad (20)$$

Eq. (18) can also be expressed as:

$$\frac{\tau_p - \tau_f}{k_{HBS} u_p - \tau_f} = \exp \left[ - \left( \frac{k_{HBS} u_p - \sigma_n \tan \varphi_{HBS}^y - c_{HBS}^y}{F_0} \right)^m \right]. \quad (21)$$

Combining Eqs. (20) and (21), Eq. (22) can be obtained as

$$\left( \frac{k_{HBS} u_p - \sigma_n \tan \varphi_{HBS}^y - c_{HBS}^y}{F_0} \right)^{m-1} = \frac{F_0}{m (k_{HBS} u_p - \tau_f)}. \quad (22)$$

Eq. (21) is taken the logarithm and the following Eq. (23) can be obtained:

$$\left( \frac{k_{HBS} u_p - \sigma_n \tan \varphi_{HBS}^y - c_{HBS}^y}{F_0} \right)^m = \ln \left( \frac{k_{HBS} u_p - \tau_f}{\tau_p - \tau_f} \right). \quad (23)$$

Multiplying both sides of Eq. (22) by the term  $\frac{k_{HBS} u_p - \sigma_n \tan \varphi_{HBS}^y - c_{HBS}^y}{F_0}$  gives:

$$\left( \frac{k_{HBS} u_p - \sigma_n \tan \varphi_{HBS}^y - c_{HBS}^y}{F_0} \right)^m = \frac{k_{HBS} u_p - \sigma_n \tan \varphi_{HBS}^y - c_{HBS}^y}{m (k_{HBS} u_p - \tau_f)}. \quad (24)$$

Noting that the same term is on the left side of Eqs. (23) and (24), Eq. (25) can be obtained by combining Eqs. (23) and (24):

$$\ln \left( \frac{k_{HBS} u_p - \tau_f}{\tau_p - \tau_f} \right) = \frac{k_{HBS} u_p - \sigma_n \tan \varphi_{HBS}^y - c_{HBS}^y}{m (k_{HBS} u_p - \tau_f)}. \quad (25)$$

By solving Eq. (25), the model parameter  $m$  is expressed as follows:

$$m = \frac{k_{HBS} u_p - (\sigma_n \tan \varphi_{HBS}^y + c_{HBS}^y)}{(\tau_f - k_{HBS} u_p) \ln \left( \frac{\tau_p - \tau_f}{k_{HBS} u_p - \tau_f} \right)}. \quad (26)$$

Finally, the model parameter  $F_0$  can be resolved by substituting Eq. (26) into Eq. (23), as given below:

$$F_0 = \frac{k_{HBS} u_p - (\sigma_n \tan \varphi_{HBS}^y + c_{HBS}^y)}{\left[ -\ln \left( \frac{\tau_p - \tau_f}{k_{HBS} u_p - \tau_f} \right) \right]^{1/m}}. \quad (27)$$

### 3.4.2 Determination of strength parameters

Data from several studies suggest that GH saturation levels and stress conditions are the dominant factors that control the macroscopic mechanical behavior of GHBSs (Miyazaki et al., 2011; Yu et al., 2011; Liu et al., 2018). Peak shear stress in this study was predicted

by the modified MC strength criterion, as written in Eq. (28):

$$\tau_p = \sigma_n \tan \phi_{\text{HBS}}^p + c_{\text{HBS}}^p, \quad (28)$$

where  $c_{\text{HBS}}^p$  and  $\phi_{\text{HBS}}^p$  denote the peak cohesion and peak internal frictional angle, respectively, of GHBSs. In this study, the representative direct shear test data offered by Liu et al. (2018) were adopted. The relationships between peak cohesion  $c_{\text{HBS}}^p$ , peak frictional angle  $\phi_{\text{HBS}}^p$ , and GH saturation  $S_{\text{GH}}$  are presented in Figs. 5 and 6. The peak cohesion  $c_{\text{HBS}}^p$  increases non-linearly with increasing GH saturation, whereas the peak friction angle  $\phi_{\text{HBS}}^p$  increases and then decreases as GH saturation increases, reaching a peak at a GH saturation level of 25%. Hence, through fitting the above experimental data, Eqs. (29) and (30) were adopted in this study to express the cohesion and internal frictional angle as a function of GH saturation  $S_{\text{GH}}$ :

$$c_{\text{HBS}}^p = 3.5S_{\text{GH}}^2 + 1.2S_{\text{GH}} + 0.066, \quad (29)$$

$$\phi_{\text{HBS}}^p = -115.5S_{\text{GH}}^2 + 64.2S_{\text{GH}} + 34.7. \quad (30)$$

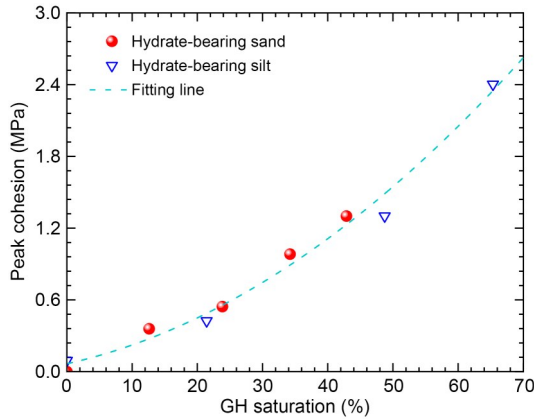


Fig. 5 Peak cohesion as a function of GH saturation  $S_{\text{GH}}$  (Liu et al., 2018)

The initial yield shear stress is used to discern whether the bonded micro-elements of GHBSs are damaged or not (Section 2.3). Therefore, determining the initial yield shear stress is fundamental for the damage evolution inside GHBSs. The relationship between the peak shear stress and initial yield shear stress of GHBSs is summarized in Fig. 7. There is a clear linear relationship between the initial yield shear stress and peak shear stress, which may be expressed simply as follows:

$$\tau_y = 0.84\tau_p - 0.1036. \quad (31)$$

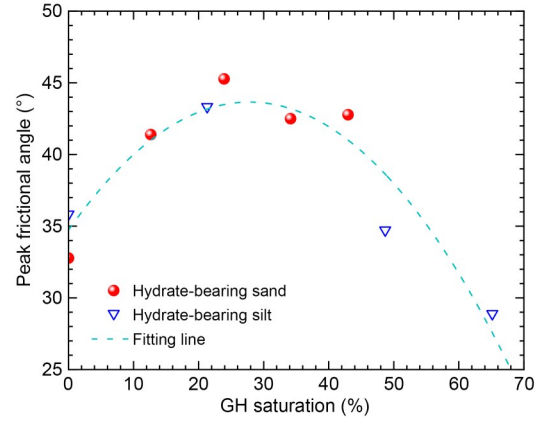


Fig. 6 Peak frictional angle as a function of GH saturation  $S_{\text{GH}}$  (Liu et al., 2018)

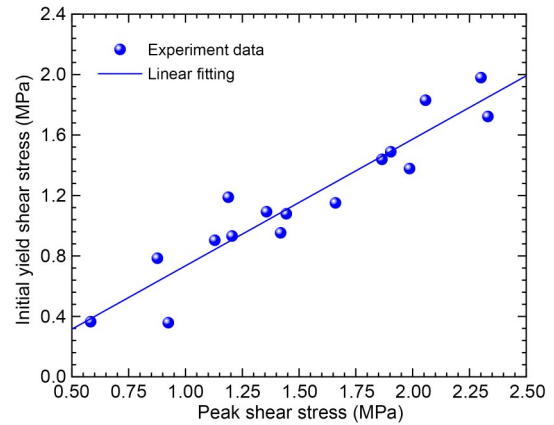


Fig. 7 Relationship between the peak shear stress and initial yield shear stress of GHBSs (Liu et al., 2018)

Fig. 8 presents the intercorrelations between the residual shear stress and normal stress. Increasing normal stress at the same GH saturation leads to an increase in the residual shear stress. The slope of the linear relationship between residual shear stress and normal stress gradually increases while the intercept is close to zero for sediments both with and without GHBSs. By increasing interparticle friction and rolling resistance, GH enhances the sediment's shear resistance since soil fabric and internal connectivity should have been destroyed at 100% shear strain. The residual shear stress  $\tau_r$  can be calculated through Eqs. (32) and (33):

$$\tau_f = M(S_{\text{GH}}) \sigma_n, \quad (32)$$

$$M(S_{\text{GH}}) = M_0 + a_4 S_{\text{GH}}, \quad (33)$$

where  $M_0$  and  $a_4$  are fitting parameters. Here,  $M_0=0.66147$ , and  $a_4=1.33788$ .

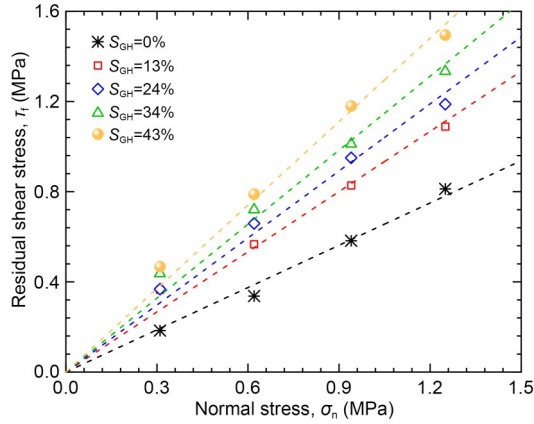


Fig. 8 Residual shear stress versus normal stress (Liu et al., 2018)

#### 4 Comparison of the proposed model and experimental results

In this section, the quality of the novel shear statistical damage model will be evaluated against representative direct shear test results. Liu et al. (2018) prepared synthetic GHBS samples with variable GH content. The influence of GH saturation level (13%, 24%, 34%, and 43%) and normal stress (0.31, 0.62, 0.94, and 1.25 MPa) on the mechanical characteristics and strength indices of GHBSs was then investigated using a series of direct shear tests. A detailed experimental description can be found in the previous study (Liu et al., 2018).

In this study, we chose the experimental data obtained by Liu et al. (2018). The model parameters  $k_{HBS}$  and  $u_p$  were determined based on experimental data at various degrees of GH saturation and normal stresses, while  $\tau_p$  and  $\tau_f$  were derived using Eqs. (28) and (32), respectively. The distribution parameters  $m$  and  $F_0$  were calculated by solving Eqs. (26) and (27). Table 2 shows the model parameters and methods used in this model. Tables 3–6 show the model parameters based on the direct shear testing that were used in the novel damage model of GHBSs to obtain the predicted results. The validity and accuracy of the novel shear constitutive model for GHBSs are validated by comparison of the predicted results with the experimental data. Fig. 9 presents the comparisons between predicted results and

Table 2 Model parameters and methods used in this model

Model parameter	Method
$k_{HBS}$	Obtained from experimental data
$\tau_p$	$\tau_p = \sigma_n \tan \varphi_{HBS}^p + c_{HBS}^p$
$u_p$	Obtained from experimental data
$\tau_y$	$\tau_y = 0.84\tau_p - 0.1036$
$\tau_f$	$\tau_f = M(S_{GH})\sigma_n, M(S_{GH}) = M_0 + a_4 S_{GH}$
$m$	$m = \frac{k_{HBS}u_p - (\sigma_n \tan \varphi_{HBS}^y + c_{HBS}^y)}{(\tau_f - k_{HBS}u_p) \ln \left( \frac{\tau_p - \tau_f}{k_{HBS}u_p - \tau_f} \right)}$
$F_0$	$F_0 = \frac{k_{HBS}u_p - (\sigma_n \tan \varphi_{HBS}^y + c_{HBS}^y)}{\left[ -\ln \left( \frac{\tau_p - \tau_f}{k_{HBS}u_p - \tau_f} \right) \right]^{1/m}}$

Table 3 Model parameters for the novel shear constitutive model under normal stress of 0.31 MPa

$S_{GH}$ (%)	$k_{HBS}$ (MPa/mm)	$u_p$ (mm)	$\tau_p$ (MPa)	$\tau_f$ (MPa)	$F_0$ (MPa)	$m$
13	0.5675	1.6145	0.5824	0.3850	1.0589	0.5622
24	1.0511	1.1100	0.8763	0.4226	1.5155	0.8877
34	2.2756	1.0843	1.2053	0.4958	1.5474	0.7894
43	4.0699	0.7470	1.4438	0.5196	1.8804	0.7468

Table 4 Model parameters for the novel shear constitutive model under normal stress of 0.62 MPa

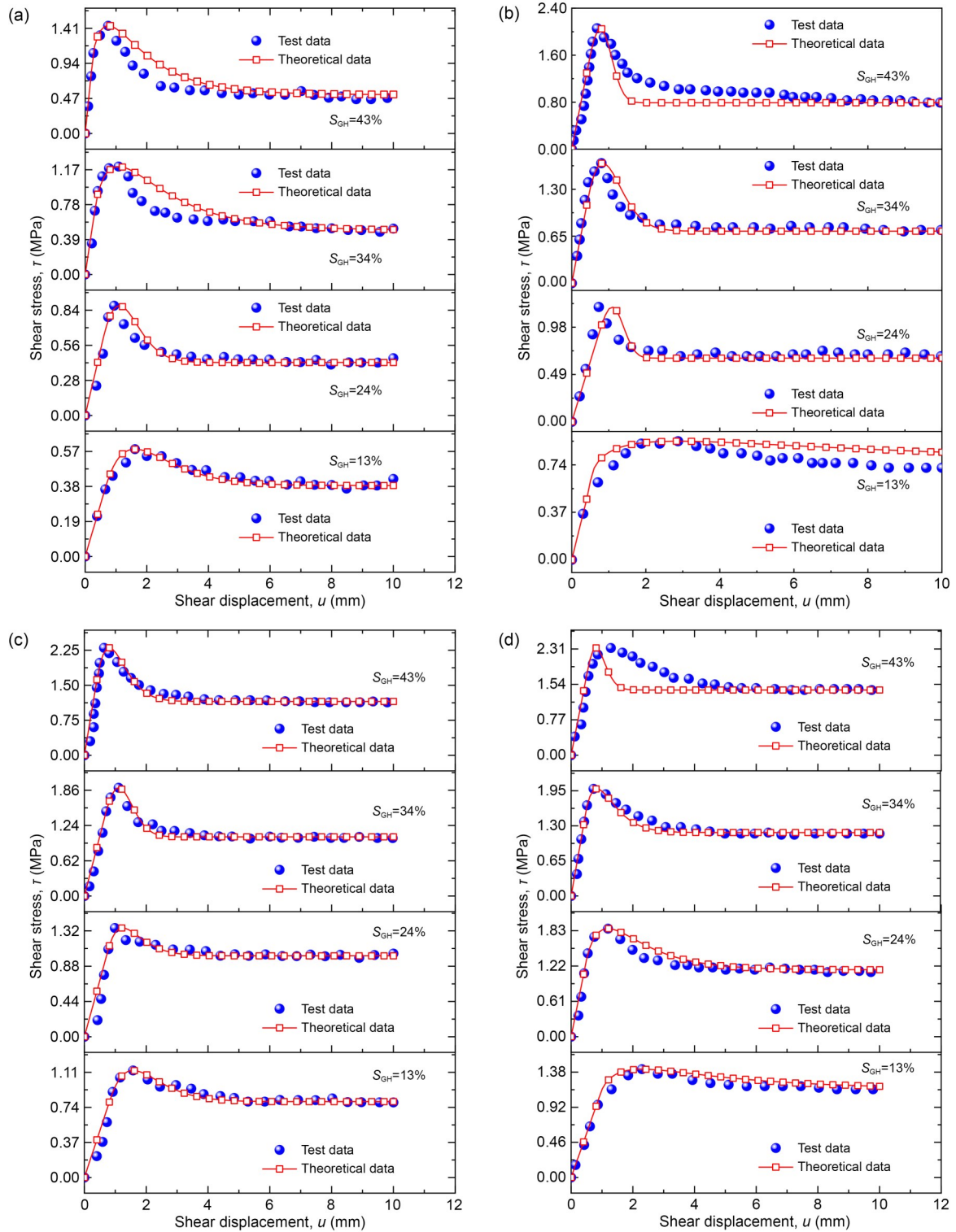
$S_{GH}$ (%)	$k_{HBS}$ (MPa/mm)	$u_p$ (mm)	$\tau_p$ (MPa)	$\tau_f$ (MPa)	$F_0$ (MPa)	$m$
13	1.1720	2.8706	0.9245	0.7200	0.2814	0.4104
24	1.2474	1.0900	1.1887	0.6590	0.8273	2.5725
34	2.6730	0.8400	1.6604	0.7203	1.8106	1.5239
43	3.2075	0.7700	2.0566	0.7893	1.8919	2.3036

Table 5 Model parameters for the novel shear constitutive model under normal stress of 0.94 MPa

$S_{GH}$ (%)	$k_{HBS}$ (MPa/mm)	$u_p$ (mm)	$\tau_p$ (MPa)	$\tau_f$ (MPa)	$F_0$ (MPa)	$m$
13	0.9851	1.5765	1.1291	0.8003	0.8595	1.1743
24	1.4075	1.2400	1.3566	1.0088	0.8155	1.1494
34	2.1097	1.1059	1.9036	1.0398	1.5722	1.8389
43	4.0075	0.8053	2.3007	1.1522	2.4084	1.3170

Table 6 Model parameters for the novel shear constitutive model under normal stress of 1.25 MPa

$S_{GH}$ (%)	$k_{HBS}$ (MPa/mm)	$u_p$ (mm)	$\tau_p$ (MPa)	$\tau_f$ (MPa)	$F_0$ (MPa)	$m$
13	1.1541	2.2951	1.4189	1.1541	0.6597	0.6188
24	2.6719	1.1944	1.8649	1.1554	1.7247	0.8548
34	3.2698	0.8360	1.9865	1.1751	1.6465	1.0972
43	3.4622	0.8025	2.3311	1.4189	1.5988	1.7361



**Fig. 9** Comparisons between experimental and predicted results for GHBSs under different degrees of GH saturation: (a) normal stress  $\sigma_n=0.31$  MPa; (b) normal stress  $\sigma_n=0.62$  MPa; (c) normal stress  $\sigma_n=0.94$  MPa; (d) normal stress  $\sigma_n=1.25$  MPa

experimental data for GHBSs under different degrees of GH saturation and normal stresses. The novel shear

constitutive model was able to predict the full shear deformation characteristics, especially the strain softening

characteristics due to bond breakage of GH by introducing the damage mechanics. The comparison of the experimental and theoretical results in Fig. 9 shows that the global performance of the novel shear damage model proposed in this paper was satisfactory.

## 5 Parametric analysis

### 5.1 Influence of $F_0$

Fig. 10 depicts how the distribution parameter  $F_0$  affects the damage evolution and shear stress–shear displacement curves of GHBSs. Fig. 10a demonstrates that as the distribution parameter  $F_0$  increases, the peak shear stress steadily rises, but the initial stiffness and residual shear stress remain unchanged. Furthermore, the same softening rate of shear stress–shear displacement curves with different distribution parameters  $F_0$  is observed, and the value of the distribution parameter

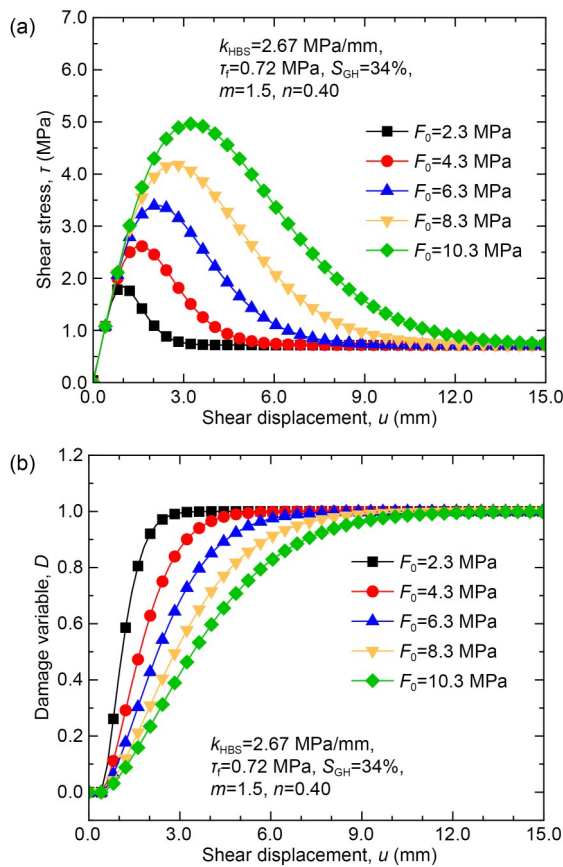


**Fig. 10** Influence of model parameter  $F_0$  on the shear response curves and damage evolution of GHBSs: (a) shear stress–displacement curves; (b) damage variable curves.  $n$  is the porosity

$F_0$  does not have any influence on the shape of the shear constitutive relation curves after the peak. The degree of bonding failure of GH, which is the microscopic origin of macroscopic strain softening, may be reflected in the distribution of damage within GHBSs. Fig. 10b depicts the damage evolution inside GHBSs with various distribution parameters  $F_0$ . The growth rate related to damage gradually decreases as the distribution parameter  $F_0$  increases, indicating that bonding failure is less likely to occur in GHBSs with a larger model parameter  $F_0$  than in those with a smaller model parameter  $F_0$ .

### 5.2 Influence of $m$

The influence of the distribution parameter  $m$  on shear stress–shear displacement curves and damage evolution inside GHBSs is depicted in Fig. 11. Fig. 11a shows that the distribution parameter  $m$  does not have any effect on the linear elastic deformation stage of GHBSs. Note that the larger the distribution parameter  $m$ , the smaller the shear stress when entering the strain softening stage. At the same time, the shear stress–shear displacement curves show a tendency for a transition from ductile to brittle failure as the distribution parameter  $m$  increases. Microscopic perspectives, such as the damage evolution of GHBSs in terms of deformation, can be used to understand the above findings. Fig. 11b shows that there is a transition point  $T$ . GHBSs with a larger distribution parameter  $m$  are less likely to suffer bonding failure prior to the transition point  $T$  than those with a smaller distribution parameter  $m$  after passing over the transition point  $T$ .

## 6 Discussion

GHBSs are inhomogeneous geotechnical materials consisting of GH particles and soil particles. Previous studies have demonstrated that the cementation failure between soil particles and GH particles inside GHBSs is the microscopic origin of the macroscopic deformation and failure processes (Wu et al., 2020). Therefore, investigating damage evolution will contribute to revealing the microscopic deformation mechanisms of GHBSs during the shearing process. The evolution equation of damage variable  $D$  may be obtained from Eq. (8), and the evolution equation of the damage rate  $R_D$  can be derived as follows:

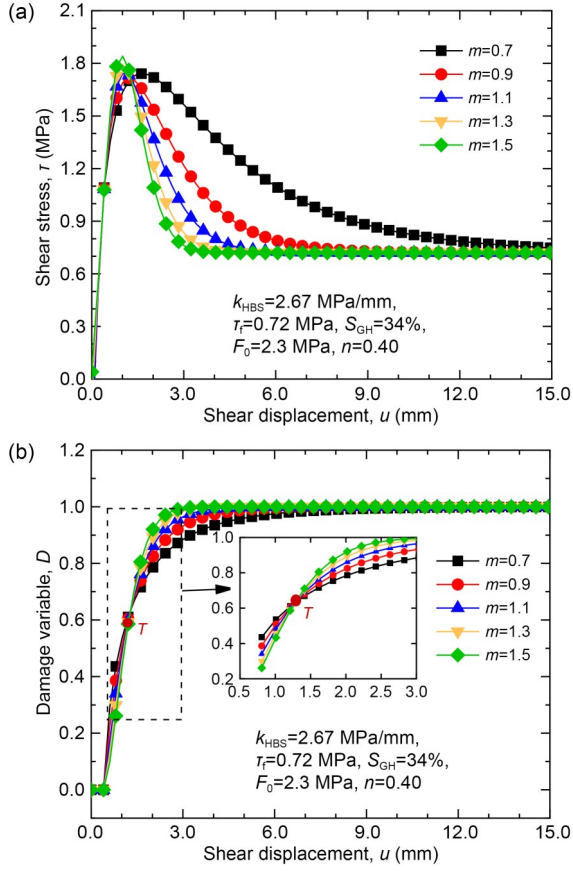


**Fig. 11** Effect of distribution parameter  $m$  on the shear response curves and damage evolution of GHBSs: (a) shear stress–displacement curves; (b) damage evolution curves

$$R_D = \frac{dD}{du} = \frac{mk_{HBS}(k_{HBS}u - \sigma_n \tan \varphi_{HBS}^y - c_{HBS}^y)^{m-1}}{F_0^m} \times \exp \left[ - \left( \frac{k_{HBS}u - \sigma_n \tan \varphi_{HBS}^y - c_{HBS}^y}{F_0} \right)^m \right] \quad (34)$$

Fig. 12 depicts the total shear stress, shear stress of the bonded elements, shear stress of the frictional elements, damage variables, and damage rate plotted against the shear displacements for GHBSs. According to the development of shear stress, as described in the first section, the total shear stress–shear displacement curve can be divided into four stages. In stage *AB*, the shear stress of bonded elements is equal to the total shear stress, while the shear stress of frictional elements is near zero, indicating that the total shear stress is supported completely by bonded elements. When entering the yield hardening stage, the shear stress borne by the frictional elements increases rapidly, while the shear stress growth rate of bonded elements

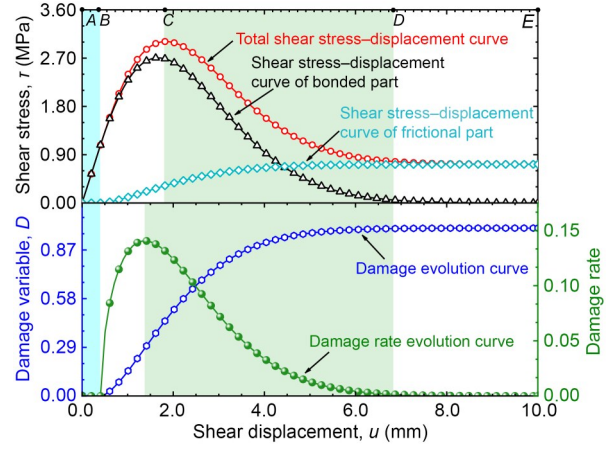


**Fig. 12** Shear stress partition and damage evolution of GHBSs under shearing process

decreases. This indicates that irreversible plastic deformation occurs inside GHBSs and bonded elements and frictional elements bear the total shear stress jointly. After passing the peak point *C*, the shear stress of the bonded elements rapidly decreases while the shear stress of the frictional elements continues to increase. When the shear displacement exceeds a certain threshold, the shear stress of the frictional elements begins to exceed the shear stress of the bonded elements. Before this threshold, the bonded elements dominate the macroscopic strength and deformation of GHBSs, while after this point the frictional elements play a dominant role in the mechanical behavior of GHBSs. Finally, the shear stress of the bonded elements decreases to zero whereas the shear stress of the frictional elements increases until it is equal to the total shear stress. It then remains constant when entering stage *DE*, indicating that the shear resistance of frictional elements provides the residual shear stress of GHBSs after destruction.

Fig. 12 also shows the damage and damage rate evolution processes inside GHBSs. The damage rate evolution pattern is a convex parabolic curve, as shown in the graph, whereas the total damage evolution curve within GHBSs has an S-shape. The damage evolution curve inside GHBSs may be separated into four stages based on damage rate evolution:

- (1) Undamaged stage: Damage variable  $D$  and damage rate  $R_D$  are both equal to zero and remain unchanged, indicating that there is no hydrate bond breakage between GH particles and sand particles, corresponding to the elastic deformation stage of the shearing process.

(2) Acceleration damage stage: The increase in damage rate leads to a rapid accumulation of damage inside GHBSs, which means that a lot of hydrate bond breakage occurs during the shearing process. In addition, when compared to the second stage of the shear deformation process, the rapid increase in damage rate is strongly related to the shear yielding of GHBSs.

(3) Damage accumulation stage: The damage rate reaches the peak point and begins to decrease gradually with increasing shear displacements, while the accumulation of damage inside GHBSs continues to increase in this stage. Note that the peak point of the damage rate curve occurs earlier than that of the shear stress curve. These findings agree with those from previous discrete element investigations and might be related to the development of shear bands.

(4) Stabilization stage: The damage rate inside GHBSs decreases to zero, while the damage variable approaches 1, after which it stops changing. This shows that the hydrate cementation in the shear bands has suffered complete breakage, enabling GH particles to enter the pore spaces, and the shear resistance between sand particles and GH particles provides residual shear stress.

## 7 Conclusions

In this paper, to predict the deformation and failure process of GHBSs in direct shear tests, a novel shear damage model based on homogenization theory and modified MC criterion is suggested. The quality and validity of the shear damage model were evaluated against representative direct shear test results. The following conclusions can be drawn from the analysis:

(1) The novel shear damage model can predict the deformation and failure characteristics, especially strain softening characteristics due to bond breakage of GH, by introducing the damage mechanics. By comparing the experimental and theoretical results, the global performance of the novel shear damage model was shown to be satisfactory.

(2) The distribution parameter  $F_0$  reflects mainly the statistical average macroscopic strength, while the distribution parameter  $m$  affects mainly the post-peak morphology of GHBSs. The shape of the whole shear stress–shear displacement curve of GHBSs is determined by the GH saturation and normal stress, which is reflected by the conjugacy of  $F_0$  and  $m$ .

(3) The shear damage model proposed in this study can better describe the damage evolution and shear stress partition mechanisms inside GHBSs during the shearing process. Additionally, it reveals the cross-scale relationship between microscopic damage evolution, mesoscopic stress partition, and macroscopic mechanical behavior. Consequently, it can more accurately reflect the nonlinear deformation and strain softening characteristics of GHBSs.

The shear damage model proposed in this paper has been verified by experimental data of GHBSs with less than 50% saturation. In the future, other direct shear test data of GHBSs with more than 50% saturation need to be adopted to evaluate the performance of the shear damage model. Additionally, it is well-known that heterogeneity is a key feature of clayey-silty GHBSs found in the South China Sea. Ren et al. (2022a, 2022b) reported that GH is first generated in small pores and then grows in large voids, resulting in heterogeneity in the spatial distribution of GH. At the same time, several studies using experiments and numerical simulation have demonstrated the important effect of the heterogeneity of particle distribution on the mechanical characteristics of GHBSs (Masui et al., 2005; Hyodo et al., 2017; Zhang JD et al., 2022). In the present shear damage model, only GH saturation was considered, not hydrate morphology and structural heterogeneity. In our ongoing work, we will attempt to capture the effects of hydrate morphology, fine content, and structural heterogeneity on the elastic properties and plastic deformation based on the meso-mechanics theory of the composite material.

## Acknowledgments

This work is supported by the Independent Innovation Research Program of China University of Petroleum (East China) (No. 27RA2215005).

## Author contributions

Hui WANG designed the research and wrote the first draft of the manuscript. Bo ZHOU revised and edited the final version.

## Conflict of interest

Hui WANG and Bo ZHOU declare that they have no conflict of interest.

## References

Bai B, Zhou R, Yang GC, et al., 2023. The constitutive behavior and dissociation effect of hydrate-bearing sediment within a granular thermodynamic framework. *Ocean Engineering*,

- 268:113408.  
<https://doi.org/10.1016/j.oceaneng.2022.113408>
- Brugada J, Cheng YP, Soga K, et al., 2010. Discrete element modelling of geomechanical behaviour of methane hydrate soils with pore-filling hydrate distribution. *Granular Matter*, 12(5):517-525.  
<https://doi.org/10.1007/s10035-010-0210-y>
- Chaouachi M, Falenty A, Sell K, et al., 2015. Microstructural evolution of gas hydrates in sedimentary matrices observed with synchrotron X-ray computed tomographic microscopy. *Geochemistry, Geophysics, Geosystems*, 16(6):1711-1722.  
<https://doi.org/10.1002/2015GC005811>
- Deusner C, Gupta S, Xie XG, et al., 2019. Strain rate-dependent hardening-softening characteristics of gas hydrate-bearing sediments. *Geochemistry, Geophysics, Geosystems*, 20(11):4885-4905.  
<https://doi.org/10.1029/2019GC008458>
- Dong L, Li YL, Liao HL, et al., 2020. Strength estimation for hydrate-bearing sediments based on triaxial shearing tests. *Journal of Petroleum Science and Engineering*, 184:106478.  
<https://doi.org/10.1016/j.petrol.2019.106478>
- Fang H, Shi K, Yu Y, 2022. A state-dependent subloading constitutive model with unified hardening function for gas hydrate-bearing sediments. *International Journal of Hydrogen Energy*, 47(7):4441-4471.  
<https://doi.org/10.1016/j.ijhydene.2021.11.104>
- Farahani MV, Hassanpouryouzband A, Yang JH, et al., 2021a. Development of a coupled geophysical-geothermal scheme for quantification of hydrates in gas hydrate-bearing permafrost sediments. *Physical Chemistry Chemical Physics*, 23(42):24249-24264.  
<https://doi.org/10.1039/D1CP03086H>
- Farahani MV, Hassanpouryouzband A, Yang JH, 2021b. Insights into the climate-driven evolution of gas hydrate-bearing permafrost sediments: implications for prediction of environmental impacts and security of energy in cold regions. *RSC Advances*, 11(24):14334-14346.  
<https://doi.org/10.1039/D1RA01518D>
- Hallinan Jr AJ, 1993. A review of the Weibull distribution. *Journal of Quality Technology*, 25(2):85-93.  
<https://doi.org/10.1080/00224065.1993.11979431>
- Hou GD, Liang DQ, Li XS, 2018. Experimental study on hydrate anti-agglomeration in the presence of rhamnolipid. *RSC Advances*, 8(69):39511-39519.  
<https://doi.org/10.1039/C8RA07215A>
- Hyodo M, Li YH, Yoneda J, et al., 2013a. Mechanical behavior of gas-saturated methane hydrate-bearing sediments. *Journal of Geophysical Research: Solid Earth*, 118(10):5185-5194.  
<https://doi.org/10.1002/2013JB010233>
- Hyodo M, Yoneda J, Yoshimoto N, et al., 2013b. Mechanical and dissociation properties of methane hydrate-bearing sand in deep seabed. *Soils and Foundations*, 53(2):299-314.  
<https://doi.org/10.1016/j.sandf.2013.02.010>
- Hyodo M, Li YH, Yoneda J, et al., 2014. Effects of dissociation on the shear strength and deformation behavior of methane hydrate-bearing sediments. *Marine and Petroleum Geology*, 51:52-62.  
<https://doi.org/10.1016/j.marpetgeo.2013.11.015>
- Hyodo M, Wu Y, Nakashima K, et al., 2017. Influence of fines content on the mechanical behavior of methane hydrate-bearing sediments. *Journal of Geophysical Research: Solid Earth*, 122(10):7511-7524.  
<https://doi.org/10.1002/2017JB014154>
- Ji YK, Hou J, Cui GD, et al., 2019. Experimental study on methane hydrate formation in a partially saturated sandstone using low-field NMR technique. *Fuel*, 251:82-90.  
<https://doi.org/10.1016/j.fuel.2019.04.021>
- Jia YG, Zhu CQ, Liu LP, et al., 2016. Marine geohazards: review and future perspective. *Acta Geologica Sinica (English Edition)*, 90(4):1455-1470.  
<https://doi.org/10.1111/1755-6724.12779>
- Jiang MJ, Chen H, Tapias M, et al., 2014. Study of mechanical behavior and strain localization of methane hydrate bearing sediments with different saturations by a new DEM model. *Computers and Geotechnics*, 57:122-138.  
<https://doi.org/10.1016/j.compgeo.2014.01.012>
- Jiang MJ, Liu J, Shen ZF, 2019. DEM simulation of grain-coating type methane hydrate bearing sediments along various stress paths. *Engineering Geology*, 261:105280.  
<https://doi.org/10.1016/j.enggeo.2019.105280>
- Kajiyama S, Hyodo M, Nakata Y, et al., 2017. Shear behaviour of methane hydrate bearing sand with various particle characteristics and fines. *Soils and Foundations*, 57(2):176-193.  
<https://doi.org/10.1016/j.sandf.2017.03.002>
- Kvenvolden KA, 1998. A primer on the geological occurrence of gas hydrate. *Geological Society, London, Special Publications*, 137:9-30.  
<https://doi.org/10.1144/GSL.SP.1998.137.01.02>
- Kvenvolden KA, 1999. Potential effects of gas hydrate on human welfare. *Proceedings of the National Academy of Sciences of the United States of America*, 96(7):3420-3426.  
<https://doi.org/10.1073/pnas.96.7.3420>
- Lai Y, Li S, Qi J, et al., 2008. Strength distributions of warm frozen clay and its stochastic damage constitutive model. *Cold Regions Science and Technology*, 53(2):200-215.  
<https://doi.org/10.1016/j.coldregions.2007.11.001>
- Lei L, Seol Y, Choi JH, et al., 2019. Pore habit of methane hydrate and its evolution in sediment matrix-laboratory visualization with phase-contrast micro-CT. *Marine and Petroleum Geology*, 104:451-467.  
<https://doi.org/10.1016/j.marpetgeo.2019.04.004>
- Li CF, Liu CL, Hu GW, et al., 2019. Investigation on the multi-parameter of hydrate-bearing sands using nano-focus X-ray computed tomography. *Journal of Geophysical Research: Solid Earth*, 124(3):2286-2296.  
<https://doi.org/10.1029/2018JB015849>
- Li DL, Wang Z, Liang DQ, et al., 2019. Effect of clay content on the mechanical properties of hydrate-bearing sediments during hydrate production via depressurization. *Energies*, 12(14):2684.  
<https://doi.org/10.3390/en12142684>
- Liu ZC, Wei HZ, Peng L, et al., 2017. An easy and efficient way to evaluate mechanical properties of gas hydrate-bearing

- sediments: the direct shear test. *Journal of Petroleum Science and Engineering*, 149:56-64.  
<https://doi.org/10.1016/j.petrol.2016.09.040>
- Liu ZC, Dai S, Ning FL, et al., 2018. Strength estimation for hydrate-bearing sediments from direct shear tests of hydrate-bearing sand and silt. *Geophysical Research Letters*, 45(2):715-723.  
<https://doi.org/10.1002/2017GL076374>
- Luo TT, Li YH, Madhusudhan BN, et al., 2020. Deformation behaviors of hydrate-bearing silty sediment induced by depressurization and thermal recovery. *Applied Energy*, 276:115468.  
<https://doi.org/10.1016/j.apenergy.2020.115468>
- Masui A, Haneda H, Ogata Y, et al., 2005. The effect of saturation degree of methane hydrate on the shear strength of synthetic methane hydrate sediments. Proceedings of the 5th International Conference on Gas Hydrates, p.657-663.
- Miyazaki K, Masui A, Sakamoto Y, et al., 2011. Triaxial compressive properties of artificial methane-hydrate-bearing sediment. *Journal of Geophysical Research: Solid Earth*, 116(B6):B06102.  
<https://doi.org/10.1029/2010JB008049>
- Miyazaki K, Tenma N, Aoki K, et al., 2012. A nonlinear elastic model for triaxial compressive properties of artificial methane-hydrate-bearing sediment samples. *Energies*, 5(10):4057-4075.  
<https://doi.org/10.3390/en5104057>
- Ng CWW, Baghbanrezvan S, Kadlicek T, et al., 2020. A state-dependent constitutive model for methane hydrate-bearing sediments inside the stability region. *Géotechnique*, 70(12):1094-1108.  
<https://doi.org/10.1680/jgeot.18.P.143>
- Ng CWW, Lau SY, Zhang Q, et al., 2023. A state-dependent constitutive model for gas hydrate-bearing sediment incorporating phase change. *Gas Science and Engineering*, 119:205102.  
<https://doi.org/10.1016/j.jgsce.2023.205102>
- Pinkert S, 2017. Rowe's stress-dilatancy theory for hydrate-bearing sand. *International Journal of Geomechanics*, 17(1):06016008.  
[https://doi.org/10.1061/\(ASCE\)GM.1943-5622.0000682](https://doi.org/10.1061/(ASCE)GM.1943-5622.0000682)
- Pinkert S, Grozic JH, Priest JA, 2015. Strain-softening model for hydrate-bearing sands. *International Journal of Geomechanics*, 15(6):04015007.  
[https://doi.org/10.1061/\(ASCE\)GM.1943-5622.0000477](https://doi.org/10.1061/(ASCE)GM.1943-5622.0000477)
- Ren JJ, Liu XH, Niu MY, et al., 2022a. Effect of sodium montmorillonite clay on the kinetics of CH<sub>4</sub> hydrate-implication for energy recovery. *Chemical Engineering Journal*, 437:135368.  
<https://doi.org/10.1016/j.cej.2022.135368>
- Ren JJ, Yin ZY, Li QP, et al., 2022b. Pore-scale investigation of CH<sub>4</sub> hydrate kinetics in clayey-silty sediments by low-field NMR. *Energy & Fuels*, 36(24):14874-14887.  
<https://doi.org/10.1021/acs.energyfuels.2c03255>
- Shen J, Chiu CF, Ng CWW, et al., 2016. A state-dependent critical state model for methane hydrate-bearing sand. *Computers and Geotechnics*, 75:1-11.  
<https://doi.org/10.1016/j.compgeo.2016.01.013>
- Skempton AW, 1985. Residual strength of clays in landslides, folded strata and the laboratory. *Géotechnique*, 35(1):3-18.  
<https://doi.org/10.1680/geot.1985.35.1.3>
- Sloan Jr ED, 2003. Fundamental principles and applications of natural gas hydrates. *Nature*, 426(6964):353-359.  
<https://doi.org/10.1038/nature02135>
- Sloan Jr ED, Koh CA, 2007. Clathrate Hydrates of Natural Gases. 3rd Edition. CRC Press, Boca Raton, USA.
- Song YC, Wang SL, Yang MJ, et al., 2015. MRI measurements of CO<sub>2</sub>-CH<sub>4</sub> hydrate formation and dissociation in porous media. *Fuel*, 140:126-135.  
<https://doi.org/10.1016/j.fuel.2014.09.086>
- Song YC, Zhu YM, Liu WG, et al., 2016. The effects of methane hydrate dissociation at different temperatures on the stability of porous sediments. *Journal of Petroleum Science and Engineering*, 147:77-86.  
<https://doi.org/10.1016/j.petrol.2016.05.009>
- Stern LA, Kirby SH, Durham WB, 1998. Polycrystalline methane hydrate: synthesis from superheated ice, and low-temperature mechanical properties. *Energy & Fuels*, 12(2):201-211.  
<https://doi.org/10.1021/ef970167m>
- Uchida S, Xie XG, Leung YF, 2016. Role of critical state framework in understanding geomechanical behavior of methane hydrate-bearing sediments. *Journal of Geophysical Research: Solid Earth*, 121(8):5580-5595.  
<https://doi.org/10.1002/2016JB012967>
- Wang H, Chen YQ, Zhou B, et al., 2021. Investigation of the effect of cementing ratio on the mechanical properties and strain location of hydrate-bearing sediments by using DEM. *Journal of Natural Gas Science and Engineering*, 94:104123.  
<https://doi.org/10.1016/j.jngse.2021.104123>
- Wang YX, Wang R, Yu JK, et al., 2023. SPF-MHBS: a stress partition constitutive framework for methane hydrate-bearing sediments. *Acta Geotechnica*, 18(4):1919-1944.  
<https://doi.org/10.1007/s11440-022-01621-6>
- Wu P, Li YH, Liu WG, et al., 2020. Cementation failure behavior of consolidated gas hydrate-bearing sand. *Journal of Geophysical Research: Solid Earth*, 125(1):e2019JB018623.  
<https://doi.org/10.1029/2019JB018623>
- Wu P, Wang HJ, Huang L, et al., 2023. Pore-scale analysis of hydrate saturation on the physical parameters of hydrate-bearing sediment with different particle shapes. *Gas Science and Engineering*, 116:205052.  
<https://doi.org/10.1016/j.jgsce.2023.205052>
- Xie SJ, Lin H, Chen YF, et al., 2020a. A damage constitutive model for shear behavior of joints based on determination of the yield point. *International Journal of Rock Mechanics and Mining Sciences*, 128:104269.  
<https://doi.org/10.1016/j.ijrmms.2020.104269>
- Xie SJ, Lin H, Wang YX, et al., 2020b. A statistical damage constitutive model considering whole joint shear deformation. *International Journal of Damage Mechanics*, 29(6):988-1008.  
<https://doi.org/10.1177/1056789519900778>
- Xu JL, Wang R, Xu CS, et al., 2023. Application and improvement of a stress partition framework-based methane

- hydrate-bearing sediment constitutive model for wide range confining stress. *Computers and Geotechnics*, 159:105463. <https://doi.org/10.1016/j.compgeo.2023.105463>
- Xu M, Song EX, Jiang H, et al., 2016. DEM simulation of the undrained shear behavior of sand containing dissociated gas hydrate. *Granular Matter*, 18(4):79. <https://doi.org/10.1007/s10035-016-0675-4>
- Yan CL, Cheng YF, Li ML, et al., 2017. Mechanical experiments and constitutive model of natural gas hydrate reservoirs. *International Journal of Hydrogen Energy*, 42(31):19810-19818. <https://doi.org/10.1016/j.ijhydene.2017.06.135>
- Yang MJ, Song YC, Jiang LL, et al., 2014. Hydrate-based technology for CO<sub>2</sub> capture from fossil fuel power plants. *Applied Energy*, 116:26-40. <https://doi.org/10.1016/j.apenergy.2013.11.031>
- Yoneda J, Masui A, Konno Y, et al., 2015. Mechanical properties of hydrate-bearing turbidite reservoir in the first gas production test site of the eastern Nankai Trough. *Marine and Petroleum Geology*, 66:471-486. <https://doi.org/10.1016/j.marpetgeo.2015.02.029>
- Yoneda J, Jin Y, Katagiri J, et al., 2016. Strengthening mechanism of cemented hydrate-bearing sand at microscales. *Geophysical Research Letters*, 43(14):7442-7450. <https://doi.org/10.1002/2016GL069951>
- Yu F, Song YC, Liu WG, et al., 2011. Analyses of stress strain behavior and constitutive model of artificial methane hydrate. *Journal of Petroleum Science and Engineering*, 77(2):183-188. <https://doi.org/10.1016/j.petrol.2011.03.004>
- Yun TS, Santamarina JC, Ruppel C, 2007. Mechanical properties of sand, silt, and clay containing tetrahydrofuran hydrate. *Journal of Geophysical Research: Solid Earth*, 112(B4):B04106. <https://doi.org/10.1029/2006JB004484>
- Zhang JD, Liu XH, Chen DY, et al., 2022. An investigation on the permeability of hydrate-bearing sediments based on pore-scale CFD simulation. *International Journal of Heat and Mass Transfer*, 192:122901. <https://doi.org/10.1016/j.ijheatmasstransfer.2022.122901>
- Zhang N, Wang HN, Jiang MJ, 2022. A mesoelastic-plastic damage model for hydrate-bearing sediments with various hydrate-growth patterns. *Ocean Engineering*, 266:112919. <https://doi.org/10.1016/j.oceaneng.2022.112919>
- Zhang XH, Lin J, Lu XB, et al., 2018. A hypoplastic model for gas hydrate-bearing sandy sediments. *International Journal for Numerical and Analytical Methods in Geomechanics*, 42(7):931-942. <https://doi.org/10.1002/nag.2772>
- Zhou M, Soga K, Yamamoto K, 2018. Upscaled anisotropic methane hydrate critical state model for turbidite hydrate-bearing sediments at east Nankai Trough. *Journal of Geophysical Research: Solid Earth*, 123(8):6277-6298. <https://doi.org/10.1029/2018JB015653>
- Zhu CQ, Zhang MS, Liu XL, et al., 2017. Gas hydrates: production, geohazards and monitoring. *Journal of Catastrophology*, 32(3):51-56 (in Chinese). <https://doi.org/10.3969/j.issn.1000-811X.2017.03.010>
- Zou ZX, Yan JB, Tang HM, et al., 2020. A shear constitutive model for describing the full process of the deformation and failure of slip zone soil. *Engineering Geology*, 276:105766. <https://doi.org/10.1016/j.enggeo.2020.105766>